JOURNAL OF GEOPHYSICAL RESEARCH, VOL. 106, NO. C10, PAGES 22,441–22,449, OCTOBER 15, 2001

Numerical study of the spatial distribution of the M_2 internal tide in the Pacific Ocean

Yoshihiro Niwa and Toshiyuki Hibiya

Department of Earth and Planetary Science, Graduate School of Science, University of Tokyo, Tokyo, Japan

Abstract. As a first step toward numerical modeling of global internal tides, we clarify the distribution of the M_2 internal tide in the Pacific Ocean using a three-dimensional primitive equation numerical model. The numerical simulation shows that energetic internal tides are generated over the bottom topographic features in the Indonesian Archipelago, the Solomon Archipelago, the Aleutian Archipelago, and the Tuamotu Archipelago, the continental shelf slope in the East China Sea, and the mid-oceanic ridges such as the Izu-Ogasawara Ridge, the Hawaiian Ridge, the Norfolk Ridge, the Kermadec Ridge, and the Macquarie Ridge. The calculated spatial patterns of the M_2 internal tide around the Hawaiian Ridge and the Izu-Ogasawara Ridge agree well with the TOPEX/Poseidon altimetric observation. The conversion rate from the M_2 surface to internal tide energy integrated over the whole model domain amounts to 338 GW (1 GW = 10^9 W), 84% of which are found to be generated over the prominent topographic features mentioned above. Reflecting the spatial distribution of the prominent topographic features in the Pacific Ocean, the energy level of the M_2 internal tide in the western and central Pacific is 2–3 orders of magnitude higher than that in the eastern Pacific. This remarkable asymmetry shows that extensive microstructure measurements in the western and central Pacific are indispensable to determining the representative value of diapycnal mixing rates in the global ocean.

1. Introduction

Internal tides are internal waves with tidal or quasi-tidal periods resulting from the interaction of barotropic tidal flow with bottom topography in a stratified ocean. A large number of previous studies focused on energetic internal tides generated over continental shelf slopes, while recent studies are more concerned with internal tides generated over bottom topographic features in the open ocean such as mid-oceanic ridges and seamounts [*Ray and Mitchum*, 1996; *Merrifield et al.*, 2001]. The surface (barotropic) to internal (baroclinic) tide conversion over such bottom topographic features is thought to be an important process leading to a sink of surface tide energy. Recently, *Egbert and Ray* [2000] and *Jayne and Laurent* [2001] both suggested that about 1 TW (1 TW = 10^{12} W), or 25–30%, of the global tidal energy dissipation occurs near bottom topographic features in the open ocean.

Internal tides also play crucial roles in the larger oceanographic context since they are thought to be associated closely with diapycnal mixing processes in the deep ocean; internal tides nonlinearly interact with background internal waves characterized by the Garrett and Munk (GM) spectrum [*Garrett and Munk*, 1972, 1975; *Munk*, 1981] with the result that part of the internal tide energy is transferred across the GM spectrum down to small mixing scales. The diapycnal mixing thus induced is believed to be an important process to controlling the strength and pattern of large-scale thermohaline circulation, because diapycnal mixing is in balance with global upwelling of deep water to maintain the abyssal stratification in the ocean interior. Actually, oceanic general circulation models have shown that the strength of the reproduced large-scale meridional overturning is very sensitive to the magnitude of the employed diapycnal diffusivity [*Bryan*, 1987]. Clarifying the global distribution of internal tides is therefore essential for an adequate parameterization of diapycnal mixing, which is indispensable for an accurate modeling of the thermohaline circulation.

Paper number 2000JC000770.
0148-0227/01/2000JC000770$09.00

Several previous studies attempted to predict the global distribution of internal tides. *Baines* [1982] formulated a two-dimensional analytical model and examined the generation of internal tides over all the major continental shelf slopes in the global ocean. *Morozov* [1995] then applied the analytical model of *Baines* [1982] to all the major submarine ridges in the global ocean. *Sjöberg and Stigebrandt* [1992] were the first to show the global distribution of the conversion rate from surface to internal tide energy based on a simplified analytical model. However, the model of *Baines* [1982] completely ignores the presence of three-dimensional irregularities along the topography, which must be taken into account in considering the generation of internal tides particularly over the continental shelf slope where the along-slope component of tidal flow is generally dominant [*Cummins and Oey*, 1997]. The model of *Sjöberg and Stigebrandt* [1992] is also a crude ad hoc extension of the theory originally developed for a silled fjord, so that the applicability to the open ocean is questionable. Recently, *Kantha and Tierney* [1997] presented the global distribution of the M_2 internal tide by analyzing the TOPEX/Poseidon altimetric data. The altimetric observation, however, has the serious problem that only a fraction of the internal tide energy can be estimated because high vertical modes have very weak sea surface expression. Despite all of these previous studies therefore we cannot expect their results to be quantitatively precise.

To clarify the global distribution of internal tides accurately,

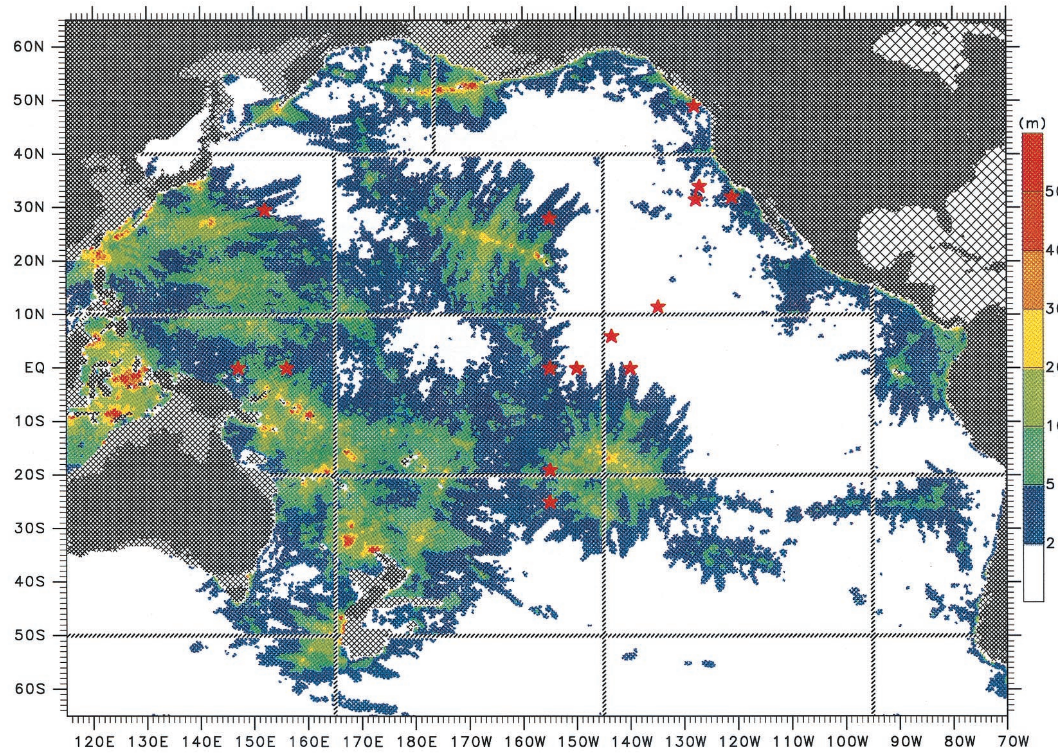

Plate 1. Model-predicted distribution of the amplitude of isopycnal vertical displacement at 1000 m depth associated with the M_2 internal tide. Small red stars denote the locations of previous microstructure measurements of diapycnal mixing rates [*Gregg*, 1998].

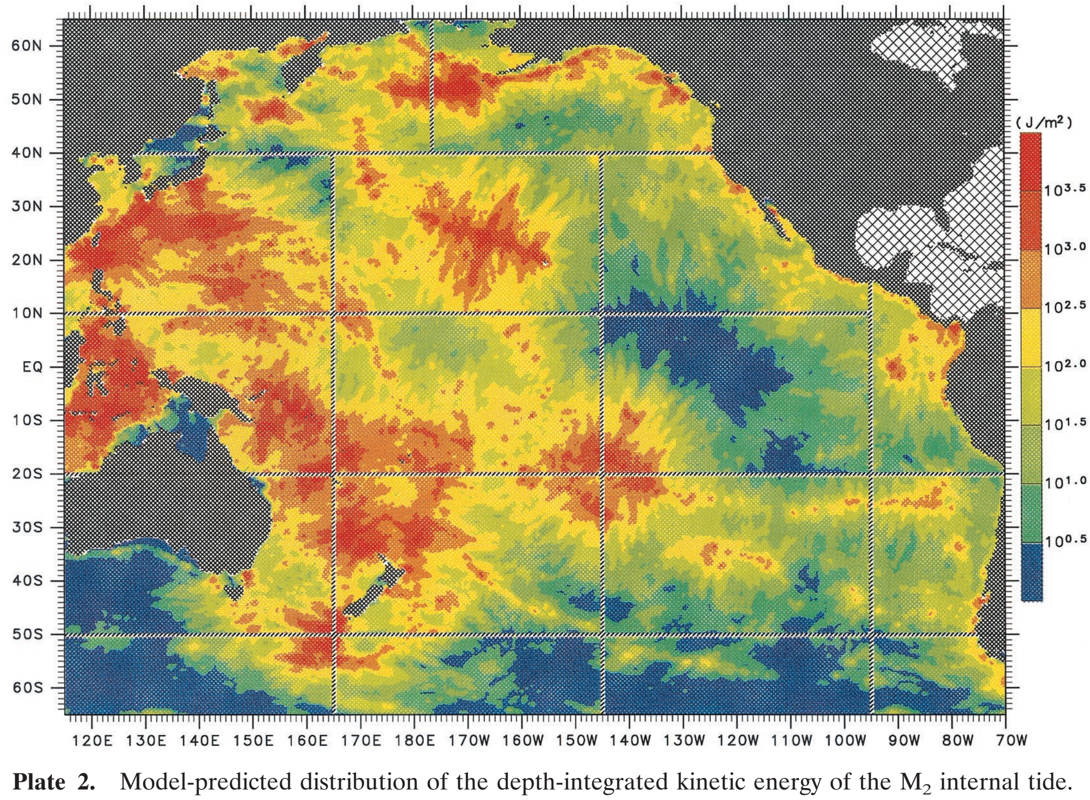

Plate 2. Model-predicted distribution of the depth-integrated kinetic energy of the M_2 internal tide.

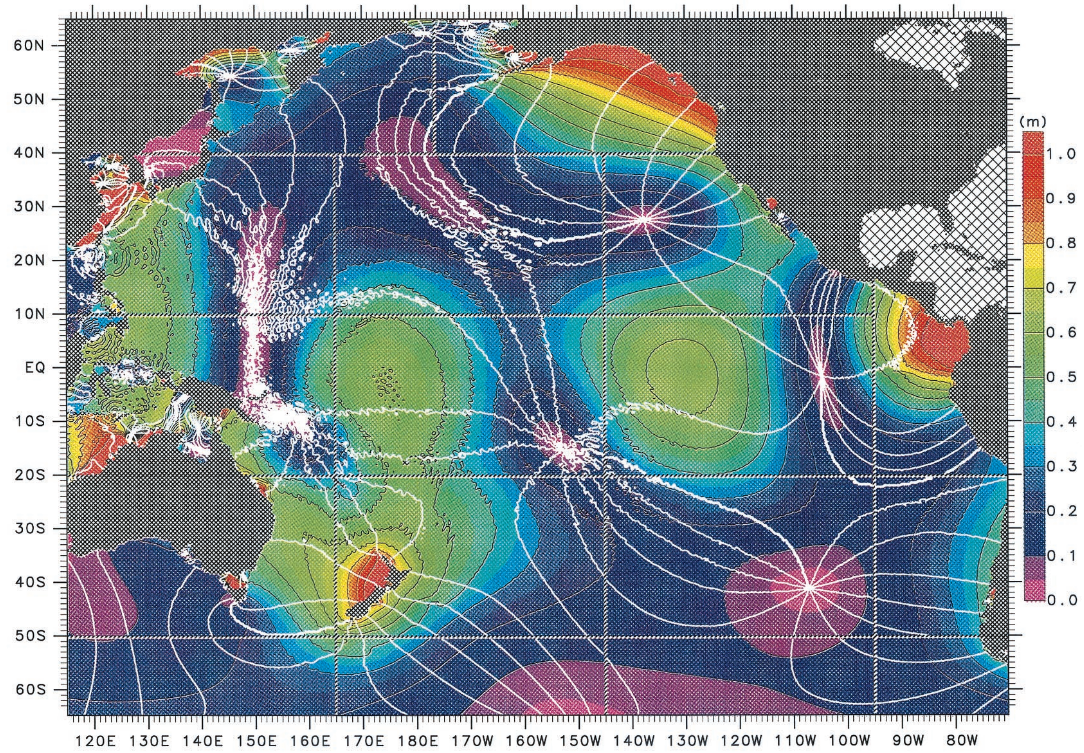

Plate 3. Corange and cophase lines for the M_2 tidal constituent in the Pacific Ocean obtained from the baroclinic simulation. The range is shown by black lines with contour intervals of 0.1 m, whereas the phase is shown by white lines with contour intervals of 30°.

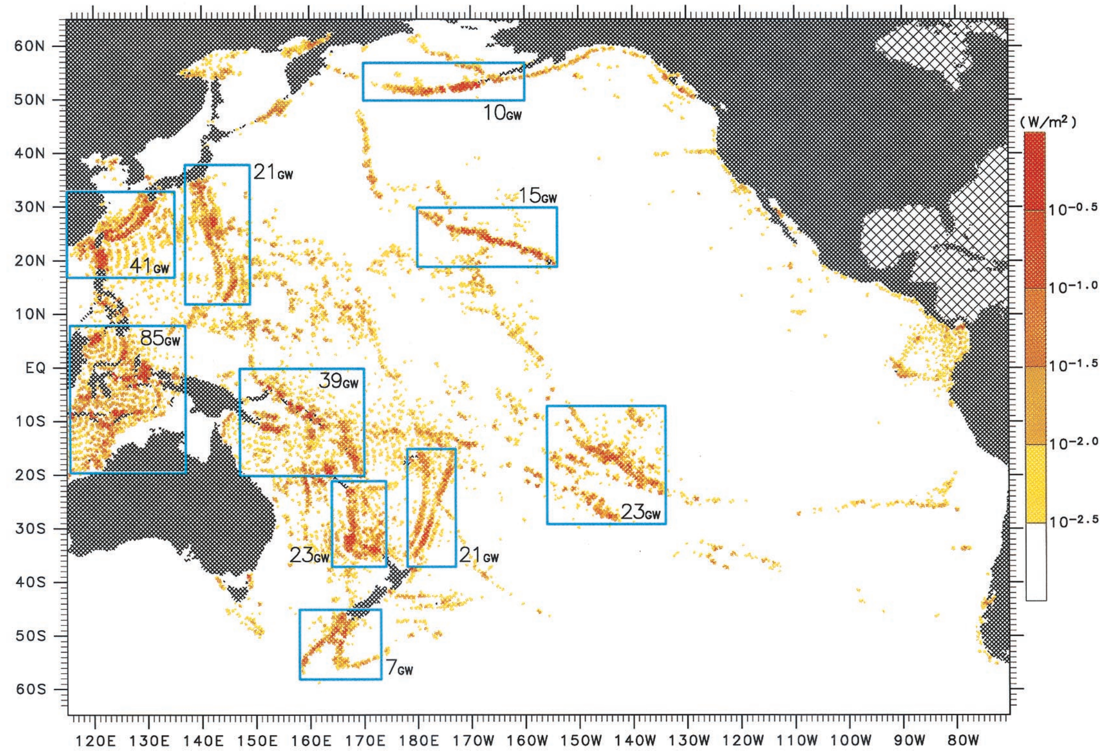

Plate 4. Model-predicted distribution of the depth-integrated M_2 mode conversion rate (for the definition, see text). The conversion rate integrated within the area including each prominent bottom topography (see Figure 1) is also shown.

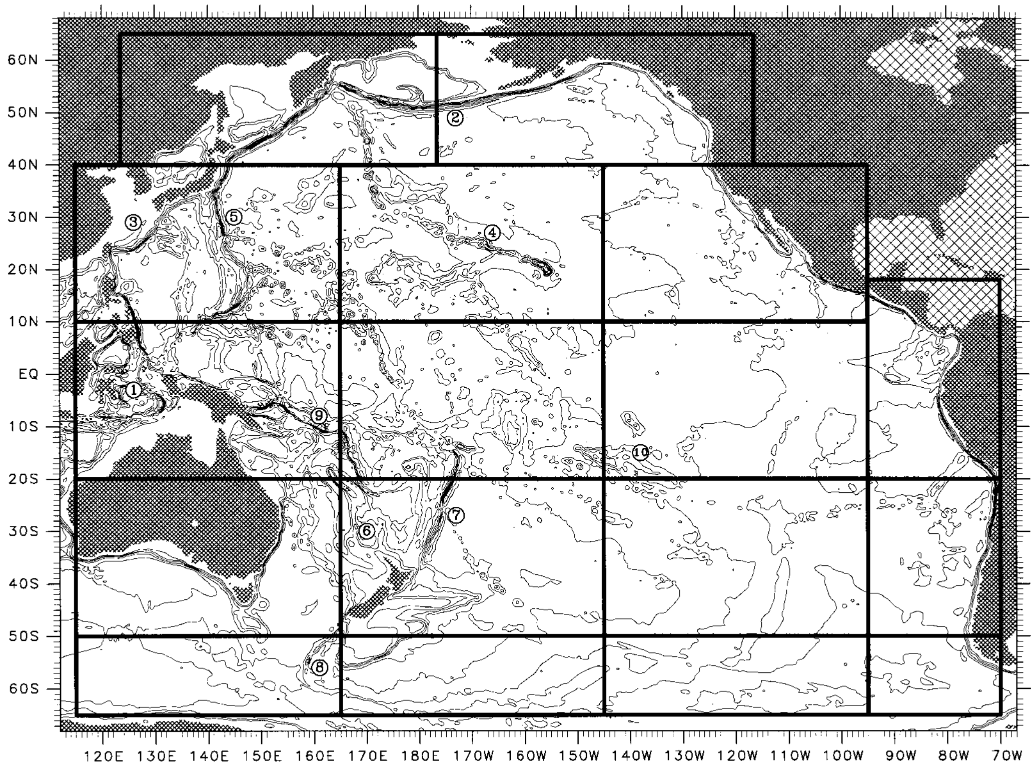

Figure 1. Model domain and bathymetry (contour interval is 1000 m). Note that the whole model domain is divided into 17 subregions for each of which numerical simulation is carried out separately. Prominent topographic features referred in the text are 1, the Indonesian Archipelago; 2, the Aleutian Archipelago; 3, the continental shelf slope in the East China Sea; 4, the Hawaiian Ridge; 5, the Izu-Ogasawara Ridge; 6, the Norfolk Ridge; 7, the Kermadec Ridge; 8, the Macquarie Ridge; 9, the Solomon Archipelago; and 10, the Tuamotu Archipelago.

a numerical modeling study based on a three-dimensional primitive equation model is most desirable. Although a number of numerical modeling studies of internal tides have been carried out, they are restricted to local oceanic regions such as over continental shelf slopes [*Cummins and Oey*, 1997; *Xing and Davies*, 1998] and mid-oceanic ridges [*Merrifield et al.*, 2001]. In the present study, as a first step toward numerical modeling of global internal tides, we clarify the distribution of the M_2 internal tide energy in the whole Pacific Ocean using a full three-dimensional primitive equation model where realistic bottom topography, density stratification, and barotropic tidal forcing are taken into account.

2. Numerical Experiment

Figure 1 shows the model domain covering the whole Pacific Ocean from 115°E to 70°W and from 65°S to 65°N. Since the computer capacity is limited, it is impossible to carry out a numerical simulation for the entire model domain using a fine grid, which is necessary to resolve internal tides. The whole model domain is therefore divided into 17 subregions, as shown in Figure 1, for each of which numerical simulation is carried out separately. In order to reproduce the surface and internal tide patterns smoothly connected with those in the surrounding subregions, a buffer region of 5° wide is assumed all around each subregion.

The governing equations are the full three-dimensional Navier-Stokes equations under the hydrostatic and Boussinesq approximations given by

$$\frac{Du}{Dt} = +fv - \frac{1}{\bar{\rho}_0}\frac{\partial}{\partial x}\left[\beta g\bar{\rho}_0\eta + \int_z^{\eta}\rho'(x, y, s)\,ds\right] + \alpha g\frac{\partial \xi}{\partial x} + A_H\nabla_H^2 u + A_V\frac{\partial^2 u}{\partial z^2} - r(u - \bar{u}), \quad (1)$$

$$\frac{Dv}{Dt} = -fu - \frac{1}{\bar{\rho}_0}\frac{\partial}{\partial y}\left[\beta g\bar{\rho}_0\eta + \int_z^{\eta}\rho'(x, y, s)\,ds\right] + \alpha g\frac{\partial \xi}{\partial y} + A_H\nabla_H^2 v + A_V\frac{\partial^2 v}{\partial z^2} - r(v - \bar{v}), \quad (2)$$

$$\frac{D\rho'}{Dt} = -\left[u\frac{\partial \rho_0}{\partial x} + v\frac{\partial \rho_0}{\partial y} + w\frac{\partial \rho_0}{\partial z}\right] + K_H\nabla_H^2\rho' + K_V\frac{\partial^2\rho'}{\partial z^2} - r\rho', \quad (3)$$

$$\frac{\partial u}{\partial x} + \frac{\partial v}{\partial y} + \frac{\partial w}{\partial z} = 0, \quad (4)$$

where t is time; (x, y, z) are defined positive eastward, northward, and upward, respectively; u, v, and w are the velocity components in the x, y, and z directions, respectively; $\bar{u}$ and $\bar{v}$

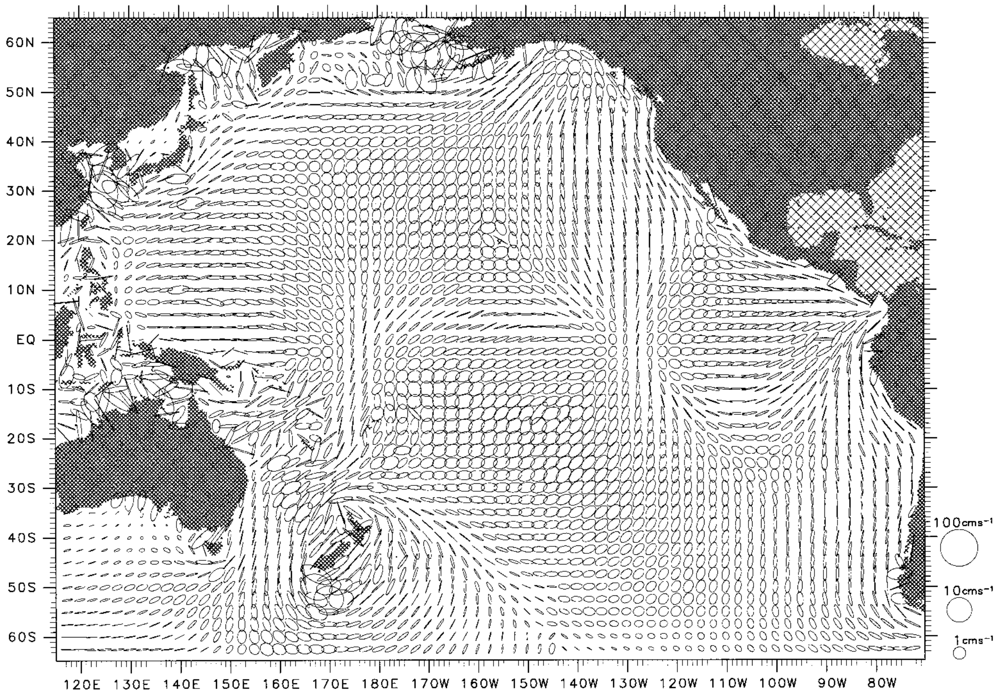

Figure 2. M_2 tidal current ellipses for the depth-averaged horizontal velocity obtained from the barotropic simulation. Note that the radius of each ellipse is logarithmically scaled.

are the depth-averaged components of u and v, respectively; $D/Dt = \partial/\partial t + u\partial/\partial x + v\partial/\partial y + w\partial/\partial z$ is the total time derivative; $\nabla_H^2 = \partial^2/\partial x^2 + \partial^2/\partial y^2$; $f = 2\Omega \sin \phi$ is the Coriolis frequency with Ω the angular velocity of the Earth's rotation and ϕ the latitude; ρ_0 is the background basic density stratification; ρ' is the water density perturbation; $\bar{\rho}_0$ is the reference water density; g is the acceleration due to gravity; η is the free-surface elevation; the factor β accounts for the effect of load tides and is assumed to be 0.946 following *Kantha* [1995] (It was pointed out by one of the reviewers that $\beta = 0.9$ is more appropriate [*Ray*, 1998]. Nevertheless, the recalculation with $\beta = 0.9$ for one subregion yields hardly noticeable difference in the calculated results, so that we retain $\beta = 0.946$ throughout this study.); ξ is the equilibrium tidal potential; the factor α multiplying ξ is the effective Earth elasticity assumed to be 0.69 following *Kantha* [1995]; horizontal eddy viscosity A_H and horizontal eddy diffusivity K_H are parameterized following the formulation of *Smagorinsky* [1963]; vertical eddy viscosity A_V and vertical eddy diffusivity K_V are parameterized following the Richardson number formulation of *Pacanowski and Philander* [1981]; and artificial linear damping coefficient r accounts for the decay of internal tide during the course of propagation caused by nonlinear interactions with the background internal waves and is assumed to be 1/5 d^{-1}, which is consistent with the estimates based on previous field observations [*Munk*, 1997] as well as with resonant interaction theory [*McComas and Müller*, 1981]. It should be noted in the above formulation that the horizontal pressure gradient associated with the background basic density stratification ρ_0 is excluded to suppress the development of geostrophic currents.

The governing equations (1)–(4) are numerically solved using the Princeton Ocean Model [*Blumberg and Mellor*, 1987] where the spherical coordinate is assumed in the horizontal and the terrain-following sigma coordinate is assumed in the vertical. The horizontal grid size is 1/16° in both latitudinal and longitudinal directions, which is about 7 km at the equator and becomes smaller in higher latitudes, and 40 vertical levels are used with higher resolutions near the ocean surface and bottom.

The model topography is constructed by averaging depth data within a 10 km radius at each grid point. As the depth data, we use the bathymetry database of *Smith and Sandwell* [1997] with resolutions of about 0.02° in latitude and about 0.03° in longitude. The background density profile at each grid point is determined by interpolating the density data calculated from the annual mean temperature and salinity data of the National Oceanographic Data Center's *World Ocean Atlas* [*Levitus and Boyer*, 1994; *Levitus et al.*, 1994].

In the present study we consider only the most dominant M_2 tidal forcing, which is applied at the open boundary by prescribing the M_2 barotropic tidal current velocity normal to the open boundary, $\bar{U}_{nb}$, using a forced gravity wave radiation condition:

$$\bar{U}_{nb} = \bar{U}_{\mathrm{tide}} \pm \sqrt{\frac{g}{H}}\,(\eta_b - \eta_{\mathrm{tide}}), \tag{5}$$

where η_b is the calculated M_2 tidal surface elevation at the open boundary; H is the total water depth at the open boundary; $\bar{U}_{\mathrm{tide}}$ and η_{tide}, both specified at the open boundary, are the M_2 barotropic tidal current velocity normal to the open boundary and the M_2 tidal surface elevation, respectively; and the positive (negative) sign is applied to the east and north (west and south) open boundary. The value of η_{tide} is determined by interpolating η_{NAO} obtained from the global barotropic tide model of *Matsumoto et al.* [2000] in which the TOPEX/Poseidon altimetric data are hydrodynamically interpolated at horizontal grid intervals of 0.5°. Then, the value of $\bar{U}_{\mathrm{tide}}$ can be determined by driving the linearized barotropic tidal model with η_{tide} specified at the open boundary for each subregion. These procedures are nearly the same as those employed by *Cummins and Oey* [1997]. To avoid the artificial reflection of internal tides at the open boundary, a flow relaxation scheme [*Martinsen and Engedahl*, 1987] is applied so that the baroclinic tidal current velocity and density perturbation both diminish as each open boundary is approached.

Furthermore, in order to reproduce the realistic surface tide field more exactly, we assimilate the interpolated altimetric data η_{NAO}. At the horizontal grid point where the value of η_{NAO} is available and also the local water depth is more than 3000 m, the calculated tidal surface elevation η_c is modified as

$$\eta' = \eta_c + \varepsilon(\eta_{\mathrm{NAO}} - \eta_c), \qquad (6)$$

where ε is a factor controlling the degree of constraint. It should be noted that the smallest possible value of ε should be assumed. If η_c is overly constrained, say, by assigning $\varepsilon \approx 1.0$, ocean surface effects of underlying internal tides cannot be retained in the model result. In the present study, $\varepsilon = 0.25$ is assumed.

The model is driven by the M_2 tidal forcing during 10 days from an initial state of rest. The calculated time series for the final 2 days are harmonically analyzed to obtain the amplitude and phase of the barotropic and baroclinic tidal responses.

3. Results

3.1. Distribution of the M_2 Internal Tide

First, we examine the barotropic response to the M_2 tidal forcing obtained by numerically integrating (1), (2), and (4) with the effect of density perturbation completely eliminated (hereinafter referred to as barotropic simulation). The amplitude and phase of the calculated barotropic surface elevation field in the whole model domain (not shown here) agree well with those of a number of previous global barotropic tidal solutions based on the analysis of the TOPEX/Poseidon altimetric data [see, e.g., *Kantha*, 1995, Plate 1]. Next, we examine the baroclinic response to the M_2 tidal forcing obtained by numerically integrating (1)–(4) with the effect of density perturbation retained (hereinafter referred to as baroclinic simulation). The internal tide field can be obtained by subtracting the solution of the barotropic simulation from that of the baroclinic simulation since the barotropic response in the baroclinic simulation is almost the same as that in the barotropic simulation.

The distribution of the isopycnal vertical displacement at 1000 m depth associated with the M_2 internal tide is shown in Plate 1, whereas the distribution of the depth-integrated kinetic energy of the M_2 internal tide is shown in Plate 2. These spatial patterns are qualitatively consistent with the M_2 internal tide field obtained by *Sjöberg and Stigebrandt* [1992], *Morozov* [1995], and *Kantha and Tierney* [1997]; energetic internal tides are generated in the coastal and marginal seas, in particular, over the bottom topographic features in the Indonesian Archipelago and the Aleutian Archipelago and over the continental shelf slope in the East China Sea. Energetic internal tides can also be found over the mid-oceanic ridges such as the Hawaiian Ridge, the Izu-Ogasawara Ridge, the Norfolk Ridge, the Kermadec Ridge, and the Macquarie Ridge as well as over the open ocean seamounts in the Solomon Archipelago and the Tuamotu Archipelago. Figure 2 shows the M_2 tidal current ellipses for the depth-averaged velocity obtained from the barotropic simulation where the radius of the ellipse is logarithmically scaled in order to emphasize the barotropic tidal ellipses in the open ocean. We can see that barotropic tidal current impinges almost perpendicularly on these prominent topographic features so that the resulting vertical velocity effectively excites energetic internal tides with the amplitudes far exceeding 10 m. Since these prominent topographic features are located mostly in the western and central Pacific, there exists remarkable asymmetry in the M_2 internal tide field in the Pacific Ocean. Actually, the energy level of the M_2 internal tide in the western and central Pacific is 2–3 orders of magnitude higher than that in the eastern Pacific.

3.2. Comparison With the TOPEX/Poseidon Altimetric Data

Plate 3 shows the corange and cophase lines for the M_2 tidal constituent obtained from the baroclinic simulation. Although the distributions of corange and cophase lines are generally the same as those in the barotropic simulation, some differences are found in the western and central Pacific where short-wavelength ($\sim$100 km) fluctuations are evident. These are attributable to ocean surface manifestations of underlying large amplitude (more than 10 m) internal tides (Plate 1).

Ray and Mitchum [1996] discussed the distribution of the M_2 internal tides around the Hawaiian Ridge by showing short-wavelength fluctuations of the M_2 tidal surface elevation extracted from the TOPEX/Poseidon altimetric data (for the details of the procedures in analyzing the TOPEX/Poseidon altimetric data, see *Matsumoto et al*. [2000]). Figure 3 shows the comparison of high-pass–filtered amplitudes of the M_2 tidal surface elevation along the TOPEX/Poseidon ground tracks over the Hawaiian Ridge obtained from the model prediction (thick solid lines) and from the TOPEX/Poseidon altimetric observation (thin solid lines). We can see that the model reproduces well the observed spatial pattern of the M_2 internal tide around the Hawaiian Ridge, indicating the validity of the present numerical simulation. Figure 4 shows the comparison in the western North Pacific near Japan where energetic M_2 internal tides are generated over the Izu-Ogasawara Ridge and the continental shelf slope in the East China Sea. It should be noted that the tidal analysis of the TOPEX/Poseidon altimetric data for 30°–40°N might be severely contaminated by intense mesoscale eddies in the Kuroshio Extension area. Otherwise, the model reproduces well the short-wavelength fluctuations of the M_2 tidal surface elevation revealed from the TOPEX/Poseidon altimetric observation over the Izu-Ogasawara Ridge. In contrast, such a good agreement is not recognized in the East China Sea where the internal tide field might be significantly modified by the strong advection effect of the Kuroshio.

3.3. Conversion Rate From the M_2 Surface to Internal Tide Energy

To examine the generation of the M_2 internal tide more quantitatively, we calculate the conversion rate from the M_2 surface to internal tide energy in the Pacific Ocean. From *Baines* [1973, equation (2.3)] we obtain the energy equation for internal tides such that

$$\frac{\partial}{\partial t}\left[(1/2)\bar{\rho}_0|\mathbf{u}'|^2 + (1/2)g(-d\rho_0/dz)^{-1}\rho'^2\right] + \nabla\cdot(p'\mathbf{u}') + D = g\rho' w_s \qquad (7)$$

where $\mathbf{u}'$ is the velocity perturbation; ρ' is the water density perturbation; p' is the pressure perturbation; w_s denotes the

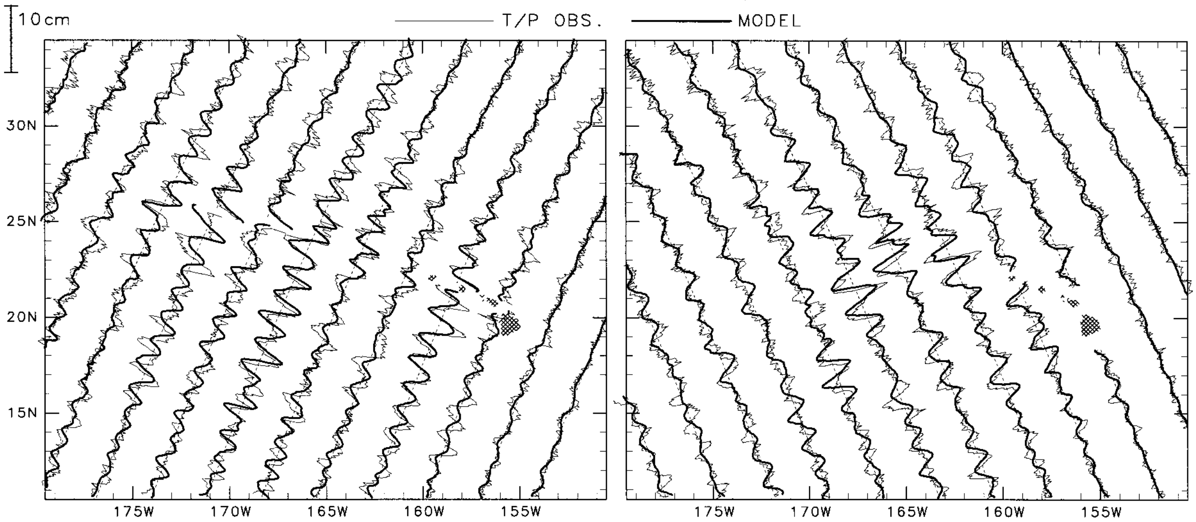

Figure 3. High-pass–filtered amplitudes of the M_2 tidal surface elevation along the TOPEX/Poseidon (left) ascending and (right) descending ground tracks over the Hawaiian Ridge obtained from the baroclinic simulation (thick solid lines) and from the TOPEX/Poseidon altimetric observation (thin solid lines).

vertical velocity resulting from the interaction of barotropic tidal current with bottom topography; and D is the generic term involving dissipative effect. In (7), $p'\mathbf{u}'$ is the energy flux that is associated with the propagation of internal tide, and $g\rho' w_s$ represents the conversion rate from surface to internal tide energy. Integrating (7) over the model domain and taking the average over one tidal period (denoted by an overbar) yields

$$\int\int \overline{p'\mathbf{u}'} \cdot d\mathbf{S} = \int\int\int g\overline{\rho' w_s}\, dV - \int\int\int \bar{D}\, dV. \qquad (8)$$

This indicates that the energy converted from surface to internal tide within the model domain is partially lost by dissipation before it radiates away through the boundaries of the model domain.

The model-predicted distribution of the depth-integrated M_2 mode conversion rate $\int g\overline{\rho' w_s}\, dz$ is presented in Plate 4 where the conversion rate integrated within the area including each prominent bottom topography (see Figure 1) is also shown. It should be noted here that ρ' and w_s are obtained from the baroclinic simulation and barotropic simulation, respectively. It is found that the M_2 mode conversion rate over these prominent topographic features sums up to 285 GW (1 GW = 10^9 W), which is 84% of that integrated over the whole model domain (338 GW). Among these topographic features the M_2 internal tide is most efficiently generated in the Indonesian Archipelago where the conversion rate reaches 85 GW. The East China Sea and the Solomon Archipelago are the second and third most important generation sites, respectively, where the conversion rate reaches about 40 GW. Although *Baines* [1982] already recognized the continental shelf slope in the East China Sea as one of the significant generators of the M_2 internal tide in the global ocean, he estimated the conversion rate to be only 1 GW, about one-fortieth that obtained here. As discussed by *Cummins and Oey* [1997], this large discrepancy implies the inapplicability of his vertical two-dimensional analytical model to tide-topography interactions in the real ocean.

The M_2 mode conversion rate over the prominent mid-oceanic ridge, namely, the Hawaiian Ridge, the Izu-Ogasawara Ridge, the Norfolk Ridge, and the Kermadec Ridge, ranges from 15 to 23 GW (see Plate 4). In particular, the M_2 mode conversion rate over the Hawaiian Ridge amounts to about 15 GW. It is interesting to note that although *Merrifield et al.* [2001] recently made quantitative estimate of the M_2 tidal energy dissipation over the Hawaiian Ridge using the three-

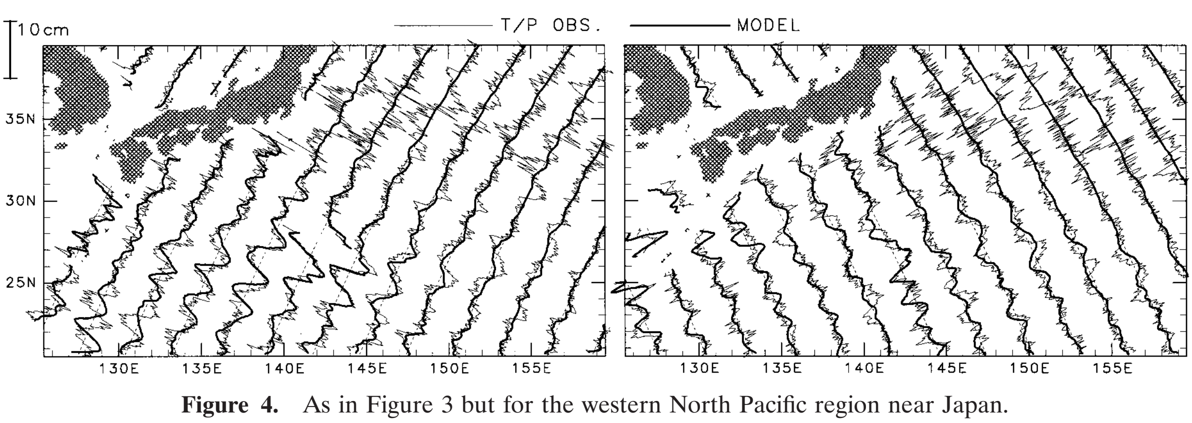

Figure 4. As in Figure 3 but for the western North Pacific region near Japan.

dimensional numerical model, their estimate corresponds to the total energy flux across the boundaries of the model domain (i.e., the left-hand side of (8)) and cannot be directly compared with our estimate here.

4. Summary and Discussion

We have investigated the spatial distribution of the M_2 internal tide in the whole Pacific Ocean using a three-dimensional primitive equation numerical model. The numerical simulation has shown that the generation of energetic internal tides is restricted over several prominent topographic features located in the western and central Pacific. Actually, the energy level of the M_2 internal tide in the western and central Pacific has been found to be 2–3 orders of magnitude higher than that in the eastern Pacific. Since part of the internal tide energy is thought to be nonlinearly transferred across the GM spectrum, ultimately contributing to abyssal mixing processes, the remarkable asymmetry of the internal tide field in the Pacific Ocean suggests that intensive abyssal mixing occurs mostly in the western and central Pacific.

The locations of previous microstructure measurements of diapycnal mixing rates [*Gregg*, 1998] are superimposed by small red stars on Plate 2. Most of the previous microstructure measurements have been carried out in the eastern North Pacific where internal tide energy available for diapycnal mixing is greatly limited. This fact might provide a possible explanation for the discrepancy between the observed and theoretically predicted diapycnal diffusivities; previously observed diapycnal diffusivity is $\sim 10^{-5}$ m^2 s^{-1}, 1 order of magnitude lower than that required to satisfy the large-scale advective-diffusive balance of the thermohaline circulation [*Munk and Wunsh*, 1998]. The possibility of this explanation is augmented by the recent numerical study of *Nagasawa et al*. [2000] showing that the wind-excited internal wave energy available for diapycnal mixing is enhanced in the western and central North Pacific. More extensive microstructure measurements are required in the central and western Pacific.

It has been shown that the conversion rate from the M_2 surface to internal tide energy in the whole Pacific Ocean amounts to 338 GW. Using the results of previous studies that the M_2 mode conversion rate in the Pacific Ocean is 46% [*Sjöberg and Stigebrandt*, 1992] and 36% [*Morozov*, 1995] of that integrated over the global ocean, we can extend the present numerical results to obtain a global estimate of the M_2 mode conversion rate, 735–939 GW, which corresponds to 31–39% of the global M_2 tidal dissipation of 2400 GW and 35–45% of the global power of 2100 GW required to satisfy the large-scale advective-diffusive balance of the thermohaline circulation [*Munk and Wunsh*, 1998]. This estimate might be somewhat ambiguous owing to the overidealized dynamical models used by *Sjöberg and Stigebrandt* [1992] and *Morozov* [1995], but it is consistent with the recent estimates of the global M_2 tidal dissipation by *Kantha and Tierney* [1997] (400–800 GW) and *Egbert and Ray* [2000] (600–800 GW), both primarily based on the TOPEX/Poseidon altimetric observation.

As discussed by *Holloway and Merrifield* [1999], the calculated results are sensitive to variations in model spatial resolution. Actually, the localized model calculations around the Hawaiian Ridge show that the total conversion rate from the M_2 surface to internal tide energy increases by 10% when the smoothing scale of the bathymetric data is reduced from 10 to 5 km and the horizontal grid spacing is decreased from 1/16° down to 1/25°, so that the resolution of the tide-topography interaction is improved. A higher-resolution numerical model incorporating more accurate bathymetry as well as the barotropic tidal forcing of all the major constituents, M_2, S_2, K_1, and O_1, is definitely required. Needless to say, the validity of the model-predicted internal tide field should be checked through a comparison with available current meter measurements over prominent topographic features as well as the TOPEX/Poseidon altimetric observations.

Acknowledgments. The authors thank K. Matsumoto for kindly providing the TOPEX/Poseidon altimetric data. Thanks are extended to John Toole and two anonymous reviewers for their invaluable comments and suggestions on the original manuscript.

References

Baines, P. G., The generation of internal tides by flat-bump topography, *Deep Sea Res*., *20*, 179–205, 1973.
Baines, P. G., On internal tide generation models, *Deep Sea Res*., *Part A*, *29*, 307–338, 1982.
Blumberg, A. F., and G. L. Mellor, A description of a three-dimensional coastal ocean circulation model, in *Three-Dimensional Coastal Ocean Models*, *Coastal Estuarine Sci*., vol. 4, edited by N. Heaps, pp. 1–16, AGU, Washington, D. C., 1987.
Bryan, F., Parameter sensitivity of primitive equation ocean general circulation models, *J. Phys. Oceanogr*., *17*, 970–985, 1987.
Cummins, P. F., and L.-Y. Oey, Simulation of barotropic and baroclinic tides off northern British Columbia, *J. Phys. Oceanogr*., *27*, 762–781, 1997.
Egbert, G. D., and R. D. Ray, Significant dissipation of tidal energy in the deep ocean inferred from satellite altimeter data, *Nature*, *405*, 775–778, 2000.
Garrett, C. J. R., and W. H. Munk, Space-time scales of internal waves, *Geophys. Fluid Dyn*., *2*, 225–264, 1972.
Garrett, C. J. R., and W. H. Munk, Space-time scales of internal waves: A progress report, *J. Geophys. Res*., *80*, 291–297, 1975.
Gregg, M. C., Estimation and geography of diapycnal mixing in the stratified ocean, in *Physical Processes in Lakes and Oceans*, *Coastal Estuarine Stud*., vol. 54, edited by J. Imberger, pp. 305–338, AGU, Washington, D. C., 1998.
Holloway, P. E., and M. A. Merrifield, Internal tide generation by seamounts, ridges, and islands, *J. Geophys. Res*., *104*, 25,937–25,951, 1999.
Jayne, S. R., and L. C. S. Laurent, Parameterizing tidal dissipation over rough topography, *Geophys. Res. Lett*., *28*, 811–814, 2001.
Kantha, L. H., Barotropic tides in the global oceans from a nonlinear tidal model assimilating altimetric tides, 1, Model description and results, *J. Geophys. Res*., *100*, 25,283–25,308, 1995.
Kantha, L. H., and C. C. Tierney, Global baroclinic tides, *Prog. Oceanogr*., *40*, 163–178, 1997.
Levitus, S., and T. P. Boyer, *World Ocean Atlas 1994*, vol. 4, *Temperature*, *NOAA Atlas NESDIS*, vol. 4, 129 pp., Natl. Oceanic and Atmos. Admin., Silver Spring, Md., 1994.
Levitus, S., R. Burgett, and T. P. Boyer, *World Ocean Atlas 1994*, vol. 3, *Salinity*, *NOAA Atlas NESDIS*, vol. 3, 111 pp., Natl. Oceanic and Atmos. Admin., Silver Spring, Md., 1994.
Martinsen, E. A., and H. Engedahl, Implementation and testing of a lateral boundary scheme as an open boundary condition in a barotropic ocean model, *Coastal Eng*., *11*, 603–627, 1987.
Matsumoto, K., T. Takanezawa, and M. Ooe, Ocean tide models developed by assimilating TOPEX/Poseidon altimeter data into hydrodynamical model: A global model and a regional model around Japan, *J. Oceanogr*., *56*, 567–581, 2000.
McComas, C. H., and P. Müller, The dynamic balance of internal waves, *J. Phys. Oceanogr*., *11*, 970–986, 1981.
Merrifield, M. A., P. E. Holloway, and T. M. S. Johnston, The generation of internal tides at the Hawaiian Ridge, *Geophys. Res. Lett*., *28*, 559–562, 2001.
Morozov, E. G., Semidiurnal internal wave global field, *Deep Sea Res*., *Part I*, *42*, 135–148, 1995.
Munk, W. H., Internal waves and small-scale processes, in *Evolution of*

Physical Oceanography, edited by B. S. Warren and C. Wunsch, pp. 264–291, MIT Press, Cambridge, Mass., 1981.
Munk, W. H., Once again: Once again-tidal friction, *Prog. Oceanogr.*, *40*, 7–35, 1997.
Munk, W. H., and C. Wunsh, Abyssal recipes, II, Energetics of tidal and wind mixing, *Deep Sea Res.*, *Part I*, *45*, 1977–2010, 1998.
Nagasawa, M., Y. Niwa, and T. Hibiya, Spatial and temporal distribution of the wind-induced internal wave energy available for deep water mixing in the North Pacific, *J. Geophys. Res.*, *105*, 13,933–13,943, 2000.
Pacanowski, R. C., and S. G. H. Philander, Parameterization of vertical mixing in numerical models of tropical oceans, *J. Phys. Oceanogr.*, *11*, 1443–1451, 1981.
Ray, R. D., Ocean self-attraction and loading in numerical tidal models, *Mar. Geod.*, *21*, 181–192, 1998.
Ray, R. D., and G. T. Mitchum, Surface manifestation of internal tides generated near Hawaii, *Geophys. Res. Lett.*, *23*, 2101–2104, 1996.
Sjöberg, B., and A. Stigebrandt, Computations of the geographical distribution of the energy flux to mixing processes via internal tides and the associated vertical circulation in the ocean, *Deep Sea Res.*, *Part A*, *39*, 269–291, 1992.
Smagorinsky, J. S., General circulation experiments with the primitive equations, I, The basic experiment, *Mon. Weather Rev.*, *91*, 99–164, 1963.
Smith, W. H. F., and D. T. Sandwell, Global sea floor topography from satellite altimetry and ship depth soundings, *Science*, *277*, 1956–1962, 1997.
Xing, J., and A. M. Davies, A three-dimensional model of internal tides on the Malin-Helbrides shelf and shelf edge, *J. Geophys. Res.*, *103*, 27,821–27,847, 1998.

T. Hibiya and Y. Niwa, Department of Earth and Planetary Science, Graduate School of Science, University of Tokyo, Tokyo 113-0033, Japan. (niwa@aos.eps.s.u-tokyo.ac.jp)

(Received December 21, 2000; revised May 18, 2001; accepted May 25, 2001.)